Exclusive seismoacoustic detection and characterisation of an unseen and unheard fireball in the North Atlantic

Stephen P. Hicks[1,✝,*], Sandro B. Matos[2,*], Adriano Pimentel[2,3], Giacomo Belli[4], Duccio Gheri[4], Maria Tsekhmistrenko[1], Kasra Hosseini[1], Wolfram H. Geissler[5], Rita Silva[3,2], Nicolau Wallenstein[2], Ana M.G. Ferreira[1].

1. Department of Earth Sciences, University College London, London, United Kingdom.
2. Instituto de Investigação em Vulcanologia e Avaliação de Riscos (IVAR), Universidade dos Açores, Ponta Delgada, Azores, Portugal.
3. Centro de Informação e Vigilância Sismovulcânica dos Açores (CIVISA), Ponta Delgada, Azores, Portugal.
4. Dipartimento di Scienze della Terra, Università degli Studi di Firenze, Italy.
5. Alfred Wegener Institute, Helmholtz Centre for Polar and Marine Research, Bremerhaven, Germany.

* Equally contributing authors

✝ Corresponding author (email: stephen.hicks@ucl.ac.uk)

Abstract

Small meteoroids that enter Earth's atmosphere often go unnoticed; their detection and characterisation rely on human observations, introducing observational biases in space and time. Acoustic shockwaves from meteoroid ablation convert to infrasound and seismic energy, enabling fireball detection using seismoacoustic methods. We analysed an unreported fireball in 2022 near the Azores, recorded by 26 seismometers and two infrasound arrays. Through polarisation analyses, array methods, and 3-D ray-tracing, we determined that the terminal blast occurred at 40 km altitude, ~60 km NE of São Miguel Island. This location matches an unidentified flash captured by a lightning detector aboard the GOES-16 satellite. The estimated kinetic energy is ~10^{-3} kT TNT equivalent, suggesting a 10^{-1} m object diameter, thousands of which enter the atmosphere annually. Our results demonstrate how geophysical methods, in tandem with satellite data, can significantly improve the observational completeness of meteoroids, advancing our understanding of their sources and entry processes.

Plain Language Summary

Every year, hundreds to thousands of small near-Earth objects, known as meteoroids, enter Earth's atmosphere. Their hypersonic entry speed and break-up can generate flashes known as fireballs and associated shockwaves that can reach the ground. However, it is only the largest objects breaking up above populated areas that we typically see or hear, or that are captured by dedicated camera systems. Many of the smaller meteoroids go unnoticed. This observational bias limits our understanding of these objects and how they enter Earth's atmosphere. Here, we report on a fireball that broke up over the Northern Atlantic Ocean in June 2022 and was recorded on a network of

seismometers that record sensitive ground motion and infrasound sensors that "hear" low-frequency sound waves. Our analyses of these data show a small (40 cm diameter) meteoroid exploded at around 40 km altitude and 60 km northeast of São Miguel Island. Crucially, a flash recorded by a lightning mapper aboard a weather satellite provides us with the exact time of the explosion. To the best of our knowledge, this event is the first documented case of a fireball detected solely by geophysical means without relying on initial reports from human observers or photographic/video evidence.

Key Points

1. We use seismic and infrasound data to characterise a previously unreported fireball over the North Atlantic Ocean in June 2022.
2. The fireball was detected by the Geostationary Lightning Mapper onboard the GOES-16 satellite, giving a precise constraint on blast time.
3. Seismoacoustic data, in tandem with satellite observations, can help to improve our observational completeness of near-Earth objects.

1. Introduction

Meteors provide valuable insights into the solar system's early history and chemical composition. These objects travel at speeds of 11–74 km/s (Ceplecha et al., 1998; Drolshagen et al., 2020), creating fireballs when they explode upon entering the atmosphere. Bright flashes are often seen by people and captured on dedicated *all-sky* cameras or more general-purpose equipment such as CCTV systems and dash-cams. Large (>1 m diameter) meteoroids, which enter Earth's atmosphere biweekly on average (Rumpf et al., 2019), generate shockwaves and an audible boom. These shockwaves, which convert into acoustic energy (Revelle, 1976), are caused by the meteoroid's high-speed atmospheric entry or by its catastrophic fragmentation, resulting in different wave propagation effects (Edwards et al., 2008).

Acoustic and coupled seismic energy from falling meteoroids can be recorded by infrasound and seismic sensors (Brown et al., 2003; D'Auria et al., 2006; Edwards et al., 2008; Ishihara et al., 2003; Langston, 2004; Pujol et al., 2005, 2006; Stich et al., 2022; Tatum, 1999; Vera Rodriguez et al., 2022; Yamada, 2021). Infrasound sensors typically record characteristic *N*-waves (Kanamori et al., 1991), whereas velocity records are *W*-shaped (D'Auria et al., 2006; Langston, 2004). These data can help reconstruct the meteoroid's blast position and its trajectory. Two main methods are commonly used. One assumes straight rays and a constant velocity of sound through the atmosphere (Ishihara et al., 2003; Kumar et al., 2017; Langston, 2004; Pujol et al., 2006; Yamada, 2021; Yamada & Mori, 2012). The other involves ray-tracing in realistic atmospheric models while accounting for wind effects (Walker et al., 2010) to reconstruct the acoustic raypath in the atmosphere (Brown et al., 2003; Hedlin et al., 2010; Stich et al., 2022). However, distinguishing point sources from moving sources is challenging, particularly with limited observations (Vera Rodriguez et al., 2022). Other factors that complicate the modelling of seismoacoustic observations include multipathing, ground-coupled precursory signals, and site effects generating variable signal durations (Stich, 2022).

Studies on meteoroids primarily rely on initial visual and/or audible human observations (Brown, ReVelle, et al., 2002; Brown et al., 2003, 2011; D'Auria et al., 2006; Hughes et al., 2022; Ishihara et al., 2003; Kumar et al., 2017; Langston, 2004; Llorca et al., 2005; Pujol et al., 2005; Stich et al., 2022; Vera Rodriguez et al., 2022; Walker et al., 2010; Yamada, 2021; Yamada & Mori, 2012), leading to an observational bias toward populated areas, such as on the continents. Observations over oceans and islands are notably scarce, particularly without *all-sky* cameras (Silber & Brown, 2014). Factors like time of day and weather conditions can also limit human observations and camera recordings. However, new satellite sensors can identify flashes caused by fireballs (Jenniskens et al., 2018; Rumpf et al., 2019), addressing some spatial-temporal biases in data collection.

On June 29, 2022, routine visual inspection of waveforms from stations in the seismic network of the Centre for Information and Seismovolcanic Surveillance of the Azores (CIVISA) reported seismic signals across the island of São Miguel at 02:06 UTC. The slow moveout of these signals eliminated an earthquake or quarry blast source (the latter highly unlikely during the night). Anomalous signals were also detected on infrasonic arrays on the islands of Graciosa and São Jorge, ~200 km to the NW of São Miguel, some 10 minutes later. However, no one had reported visual or audible observations. We further searched social media and explored the possibility of obtaining webcam footage; however, we found no reports of fireballs. The local astronomical observatory Observatório Astronómico de Santana, Açores, located on the North coast of São Miguel also had no records of the event. Skies were clear that night, as confirmed by an infrared satellite image at 02:00 UTC (Figure S1).

Here, we study this suspected but previously unreported fireball in the Azores region using seismological, infrasonic, and satellite data. To the best of our knowledge, this event is the first documented case of a fireball detected solely by geophysical means without relying on initial reports from human observers or photographic/video evidence. The implications of our study could enhance global datasets of near-Earth objects, thus presenting new opportunities for improving our understanding of these phenomena.

2. Seismic data and waveform characteristics

To investigate this event, we analysed all available seismic data from the Azores, primarily from CIVISA, the Azores seismo-volcanic monitoring agency (network code: CP) and the Portuguese National Seismic Network (network code: PM) (Instituto Português do Mar e da Atmosfera, I.P., 2006) (Figure 1a). These networks comprise a combination of single-component short-period, three-component short-period, and three-component broadband seismometers. Manual assessment of the waveforms shows that all but one of the 23 stations on São Miguel (Figure 1b & Figure 2a) recorded the event.

We picked arrival times at the onset of the impulsive, higher frequency and higher-amplitude waveform peak. The earliest arrival was at station PM.BART on the East coast of São Miguel, with progressively later arrivals towards the West (Figure 1b). Concentric isochrones emanate from NE São Miguel (Figure 1b). We estimated the direction of the source using polarisation analysis, assuming the seismic signals likely originated from an incident acoustic wave (Langston, 2004), with most stations showing elliptical horizontal particle motions (Figure 2a). We computed polarisation azimuths (Flinn, 1965) from a window commencing at the picked onset time that captures the highest amplitude arrivals (~2 s for most stations), within the frequency range of 2–6 Hz, with 1 s windows overlapping every 0.1 s. Stations in East São Miguel have NE azimuths, while stations to the West and North have ENE-directed azimuths (Figure 1b). These directions are roughly perpendicular to the nearest isochrones and consistent with a source located NE of São Miguel.

Many of the seismic waveforms exhibit a *W*-shape (i.e., with downward first-motions) (Figure 2a), which is characteristic of a pressure *N*-wave on a velocity trace, suggesting a hypersonic or supersonic source (D'Auria et al., 2006; Ishihara et al., 2003). The recorded signal is strongest in the frequency range of 1.5–8.0 Hz (Figure 2a), with less signal at audible frequencies (>20 Hz). There are substantial variations in waveform characteristics across São Miguel. The peak ground velocities vary greatly (Figure 2a). Signal durations also vary widely, ranging from 1.5 s at PM.PGRON to 18.4 s at CP.FAC (Figure 2a). Some waveforms appear highly monochromatic (e.g., CP.PVER), while others show hints of dispersion (e.g., PM.SM001). We found no clear correlation between waveform characteristics and station location, underlying geology, or elevation.

We only found obvious seismic signals from São Miguel Island, which aligns with previous observations of similar events within a limited area of ~100 km^2 (D'Auria et al., 2006; Stich et al., 2022). However, we found weak signals with low signal-to-noise ratios at four stations on Terceira Island, ~150 km to the NW (Figure 1a), with arrival times consistent with the moveout velocity observed elsewhere (Figure 3). Two stations on São Miguel (PM.BART; PM.PGRON) recorded a low-frequency precursory emergent onset lasting 0.5-1.5 s (Figure 2a).

3. Infrasound observations and array processing

We analysed data from multiple infrasound stations in the Azores (Figure 1a). The event was captured by the IS42 infrasonic array of the CTBTO's International Monitoring System on Graciosa Island, by a portable infrasonic array (SJ1) installed on São Jorge Island, as well as by a single infrasound sensor (II.CMLA) colocated with a seismometer on São Miguel. For further information about these arrays, refer to Text S1.

At II.CMLA, a short duration (~1 s) high-frequency (~10 Hz) infrasound signal with a maximum peak-to-peak amplitude of 2.9 Pa is observed (Figure 2a). However, the wavetrain is internally complex (Silber & Brown, 2014), consisting of at least four *N*-wave cycles, potentially superimposed onto a longer-period, broader *N*-wave. In contrast, arrays IS42 and SJ1 on the other islands recorded two main signals with similar amplitudes (Figure 2b). The first signal arrived ~11 mins after the earliest seismic arrival on São Miguel. The two occur two mins apart (125 s at SJ1; 103 s at IS42). These signals are more diffuse, longer in duration, lower in frequency (1.5–4 Hz), and weaker (maximum peak-to-peak amplitude ~1 Pa) than the signal on São Miguel. The arrival times of the first signal align closely with the moveout of seismic arrivals from São Miguel and Terceira, with a velocity near the speed of sound in air (Figure 3).

We used a multi-channel cross-correlation method (Ulivieri et al., 2011), to determine back-azimuth and apparent velocity (Figure 2b; Figure S7-S8). We processed 0.5–10 Hz bandpass filtered infrasound data, utilising 5 s moving windows with 99% overlap. For IS42, the back-azimuths of the two arrivals are 109.5° (±3.8°) and 109.1° (±5.1°). At SJ1, the back-azimuths are 100.1° (±1.5°) and 99.0° (±2.0°). These back-azimuths align with a source located NE of São Miguel, consistent with the seismic arrivals and polarisations. Both arrays also show a weak third arrival with a back-azimuth similar to the preceding signals, approximately two minutes after the second arrival. All apparent velocities are on the order of 300–400 m/s.

4. Source location and meteor trajectory model

4.1. Probabilistic azimuth-based location

We estimated the source location using seismic horizontal polarization directions (Figure 1b) and back-azimuths from the first signal analyzed in the IS42 and SJ1 infrasound arrays (Figure 2b). To calculate the location probability density function (PDF), we considered the 1σ back-azimuth uncertainties and computed PDFs for each back-azimuth on a 2-D grid. By multiplying these individual PDFs, we determined the maximum likelihood location and associated error ellipse (Stähler et al., 2022). Figure S2 displays the resulting PDF, while Figure 4a shows the 80% uncertainty ellipse. The primary source location uncertainty lies in the NW-SE direction, as the azimuth observations concentrate towards the West and SW due to network geometry and island geography. The maximum likelihood location lies approximately 42 km NNE of the NE coast of São Miguel.

4.2. Constant acoustic velocity source model

Using a constant-velocity, straight-ray approximation, we derived a first-order source and trajectory model. This approach has been previously employed in studies of fireballs recorded by seismic networks (Che et al., 2016; Ishihara et al., 2003; Kumar et al., 2017; Yamada, 2021; Yamada & Mori, 2012). By optimizing the source parameters using the Genetic Algorithm (Kumar et al., 2017) and considering all recorded arrival times, we determined the origin time, 3-D source position, trajectory azimuth and inclination angle, and meteoroid velocity. To improve optimization, our polarization analysis results constrained the source position range (Table S1).

Our best-fitting solution has an overall RMS arrival time misfit of 2.6 s. The horizontally-projected position closely aligns with the probabilistic location based on azimuths, falling within the 80% confidence interval (Figure 4a) and only 8 km from the maximum likelihood location. The source origin time is 02:02:38.8, with an elevation of 61 km, trajectory azimuth of 250°, and inclination of 61°. These initial parameters suggest that a meteoroid likely caused the observed seismoacoustic signals, rather than other possible sources such as an earthquake, quarry blast or thunderstorm. However, with the source lying outside our observation network, the trajectory parameters are weakly constrained, with interdependencies and tradeoffs among several parameters like elevation and origin time (Edwards et al., 2008; Yamada & Mori, 2012).

A more precise source position can be obtained using ray-tracing methods based on infrasound array data. However, these methods depend on an independently constrained origin time for the fireball (Belli et al., 2021).

4.3. Constraints from satellite data

Since the 2022 Azores meteoroid was not visually observed or captured on video, its timing and trajectory remain uncertain, causing tradeoffs with source position and limiting detailed analysis of the seismoacoustic data. To gather additional evidence, we examined data from the Geostationary Lightning Mapper (GLM) on the GOES-16 weather satellite. The GLM records transient light events at 500 fps with a resolution of 8–14 km (Rumpf et al., 2019). The minimum brightness detection is visual magnitude 14x (twice as bright as a full moon), so fireballs can be detected by the GLM (Jenniskens et al., 2018; Rumpf et al., 2019). We searched for flashes between 01:45 and 02:25 UTC on 2022/06/29, ~20 mins before and after our modelled source time (Figure S3). We identified a positive detection at 02:02:10.87. The GLM flash occurred 236 s before the first seismic wave arrival at PM.BART, 28 s earlier and 93 km NE of our modelled source time using the constant-velocity, straight-ray approximation (Figure 4a). Infrared satellite data confirms minimal cloud cover in the area at the time, ruling out lightning as a source for the detection (Figure S1).

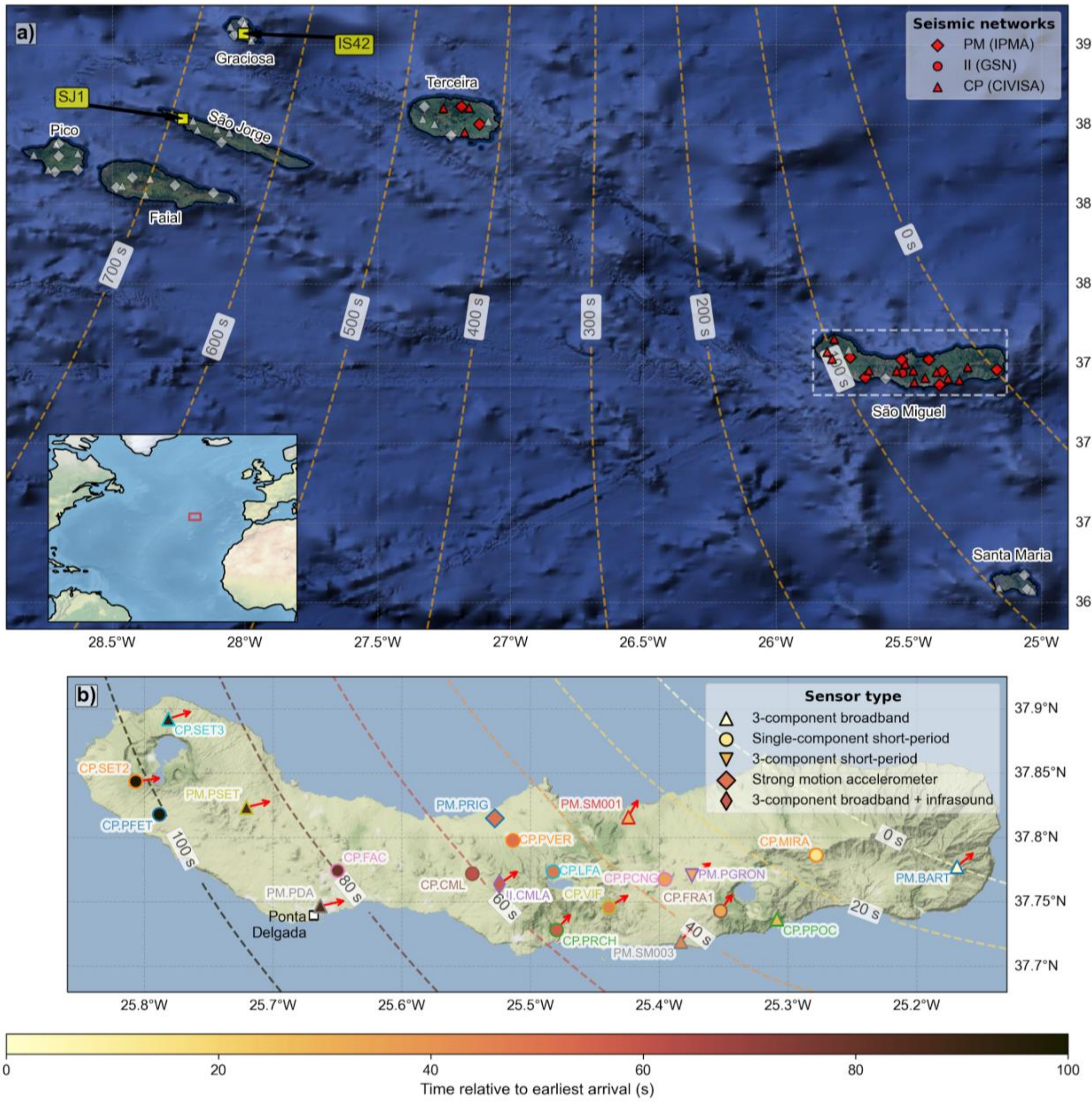

Figure 1. (a) Map of the central and eastern islands of the Azores (Pico, Faial, São Jorge, Graciosa, Terceira, São Miguel, and Santa Maria) showing seismic stations (triangles) and infrasound stations/arrays (yellow squares). Positive fireball detections are in red while negative detections are in white. Orange dashed contour lines represent interpolated relative isochrons using continuous curvature splines, relative to the first arrival at PM.BART. The inset map shows the extent of the main map (red box) in the North Atlantic Ocean. The white dashed line shows the spatial extent of (b). (b) Map of seismic stations on São Miguel Island that recorded the shockwave arrival. Station labels and symbol outlines correspond to those in Figure 2. Station symbol fills are colour-coded according to their arrival time relative to the first arrival at PM.BART. Red arrows indicate the best-fitting source azimuth from polarisation analysis **(Flinn, 1965)**.

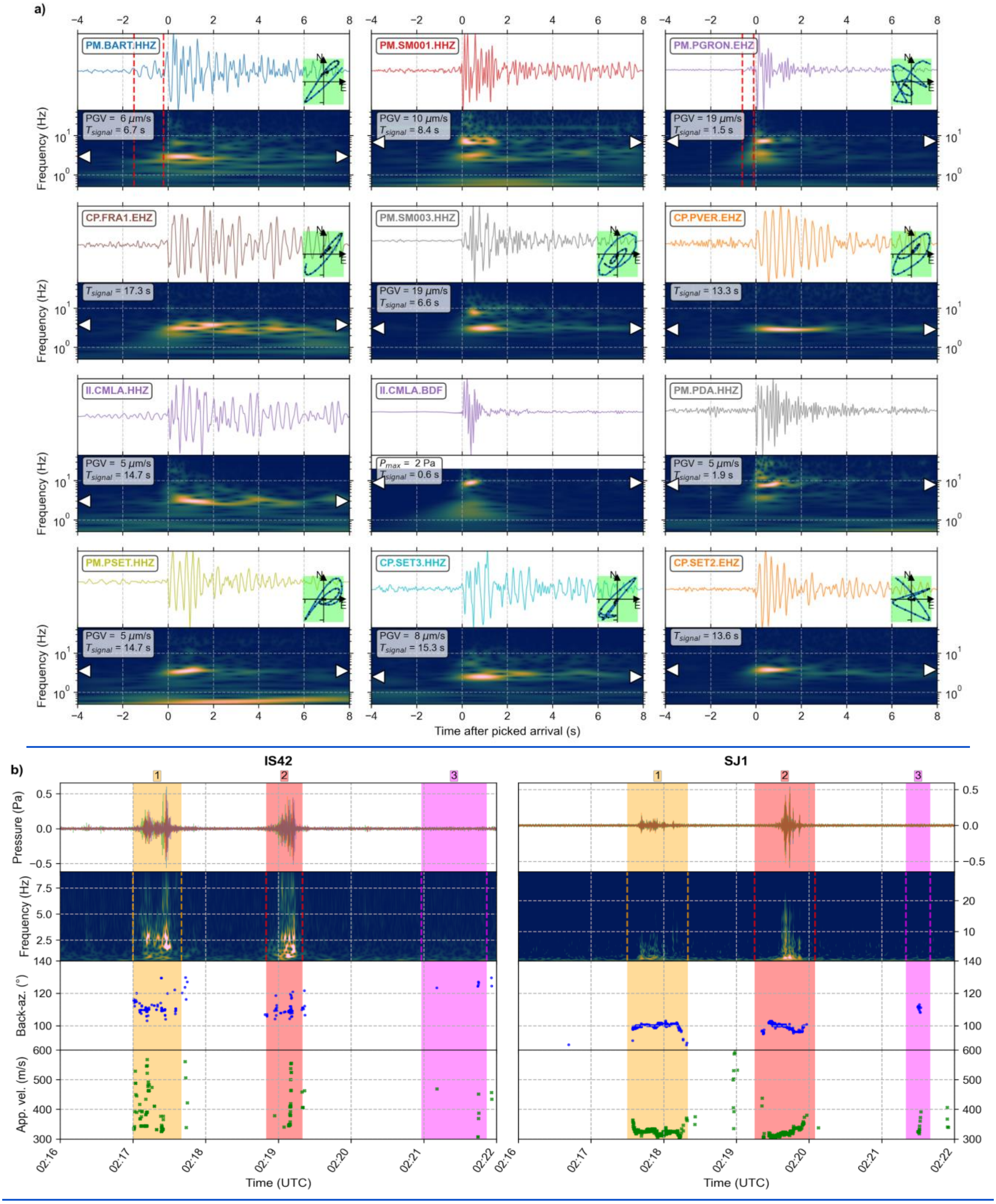
a)
PM.BART.HHZ
PGV = 6 μm/s
T_signal = 6.7 s
PM.SM001.HHZ
PGV = 10 μm/s
T_signal = 8.4 s
PM.PGRON.EHZ
PGV = 19 μm/s
T_signal = 1.5 s
CP.FRA1.EHZ
T_signal = 17.3 s
PM.SM003.HHZ
PGV = 19 μm/s
T_signal = 6.6 s
CP.PVER.EHZ
T_signal = 13.3 s
II.CMLA.HHZ
PGV = 5 μm/s
T_signal = 14.7 s
II.CMLA.BDF
P_max = 2 Pa
T_signal = 0.6 s
PM.PDA.HHZ
PGV = 5 μm/s
T_signal = 1.9 s
PM.PSET.HHZ
PGV = 5 μm/s
T_signal = 14.7 s
CP.SET3.HHZ
PGV = 8 μm/s
T_signal = 15.3 s
CP.SET2.EHZ
T_signal = 13.6 s
N
E
Frequency (Hz)
Time after picked arrival (s)
b)
IS42
SJ1
1
2
3
Pressure (Pa)
Frequency (Hz)
Back-az. (°)
App. vel. (m/s)
Time (UTC)
02:16
02:17
02:18
02:19
02:20
02:21
02:22

Figure 2: a) Z-component seismic waveforms from São Miguel (filtered 1.5–12 Hz) and infrasound waveform of II.CMLA.BDF (0.5 Hz highpass), with spectrograms below. Colours correspond to Fig. 1. Green insets display horizontal particle motions in 0.7 s windows. The frequency at peak-ground velocity (PGV) is indicated by white arrowheads. Signal duration, defined by 20% of the peak waveform envelope amplitude **(Stich et al., 2022)** is provided. Precursory signals on PM.BART & PM.PGRON are marked by vertical red lines. b) Infrasound waveforms with computed array parameters. Three distinct signals are represented by coloured strips.

Since the Azores lie at the edge of GOES-16's line-of-sight coverage, we considered parallax errors in the geolocation of the flash. While automatically-processed data from GLM considers parallax errors at typical lightning heights (up to 20-30 km at the edge of line-of-sight) (Virts & Koshak, 2020), emitters at greater heights, potentially including fireballs (Edwards et al., 2006; Gao & Mathews, 2015; Halliday et al., 1989), may see greater horizontal shifts (Rumpf et al., 2019). As the horizontal distance from the satellite subpoint increases, there is a higher chance that GLM will geolocate a flash farther away than its actual position (Virts & Koshak, 2020). We, therefore, calculated parallax corrections using *SatPy* (Raspaud et al., 2023) and found that source heights of 20–40 km matched the source position from the straight-ray modelling and polarisation analysis within 20 km distance (Figure 4a).

4.4. Integrated seismoacoustic-satellite source model

Using the independently derived origin time from the GLM, we can reconstruct a more precise source position by employing 1-D ray-tracing in a realistic atmosphere velocity model (Belli et al., 2021). To create this model, we utilised 2.5° resolution data from the National Centers for Environmental Prediction and employed the AVOG2S software (Schwaiger et al., 2019) to extend climatological data up to the thermosphere. The velocity model is based on a 1-D vertical atmospheric profile (Figure S4) centred above Mosteiros on the West coast of São Miguel. The model consists of air temperature, air density and wind velocity, up to an altitude of 180 km (Figure S4). The model has a vertical resolution of 1 km in the first 20 km and 2.5 km between 20–180 km.

From the infrasound back-azimuths and apparent velocities, we determined raypaths from the receiver back to the source. By comparing arrival times and the origin time from the GLM (02:02:10.87 UTC), the source position was calculated along the raypath (Belli et al., 2021). We applied this process separately for SJ1 and IS42 arrays, resulting in source positions only ~11 km apart (Figure 4a). The final source location is given as the average of these two positions: at 38.25°N, 24.86°W, 37.0 km altitude (16 km NE of the straight-ray and maximum likelihood azimuthal-based positions), and only 11 km away from the parallax-corrected flash position assuming an elevation of 30 km (Figure 4a). We then applied 3-D ray-tracing with InfraGA (Blom & Waxler, 2012) to this final source position to refine the raypaths and predict the arrival times at all stations that recorded the fireball event in São Miguel, Terceira, Graciosa and São Jorge (Figure 4b). Predictions are within ~10 s of all arrival time observations (Figures 3 & 4).

The 3-D raypaths (Figure 4b) demonstrate that the multiple signals at SJ1 and IS42 result from infrasonic multipathing from a single point source rather than multiple sources along the fireball trajectory. Seismic and infrasound arrivals on São Miguel are from direct stratospheric paths, while the weaker arrivals on Terceira are from rays guided by stratospheric winds through a high-speed, low-attenuation layer (Drob et al., 2003; de Groot-Hedlin et al., 2011). The first infrasound arrivals at IS42 and SJ1 are also direct stratospheric-ducted rays. Conversely, secondary arrivals at IS42 and SJ1 are modelled as stratospheric-ducted rays with a surface reflection. Finally, the weak third infrasound arrival reflects at the base of the thermosphere (Figure 4b), where strong attenuation explains the low amplitude (Figure 2b) (Ott et al., 2021).

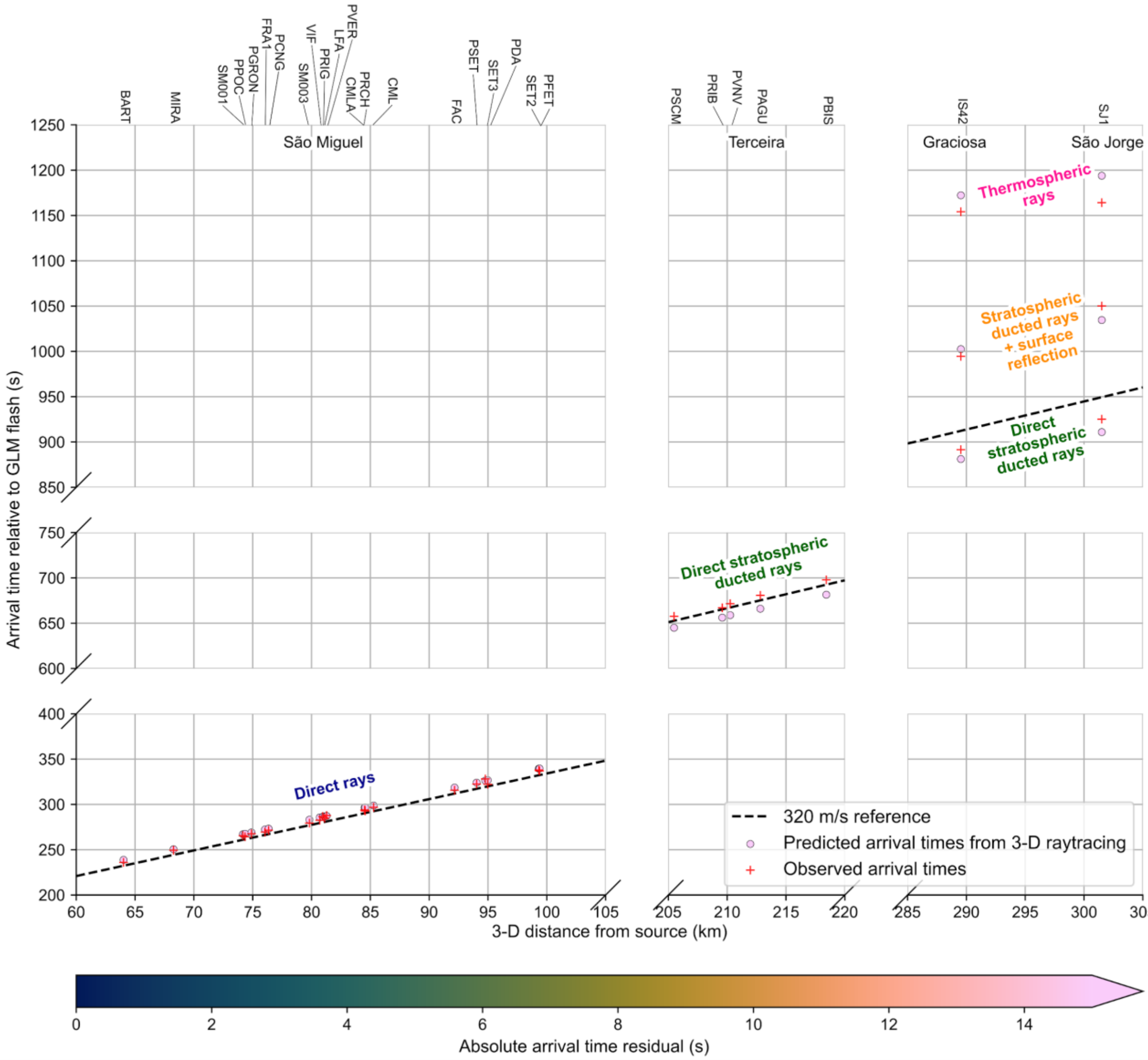

Figure 3: Observed versus predicted arrival time moveout using 3-D ray-tracing (Figure 4b) relative to the origin time constrained by the flash detected by the Geostationary Lightning Mapper (GLM). The source position comes from 3-D ray-tracing of infrasound array data. Predicted arrival times are coloured according to their residuals. Station labels are given along the top.

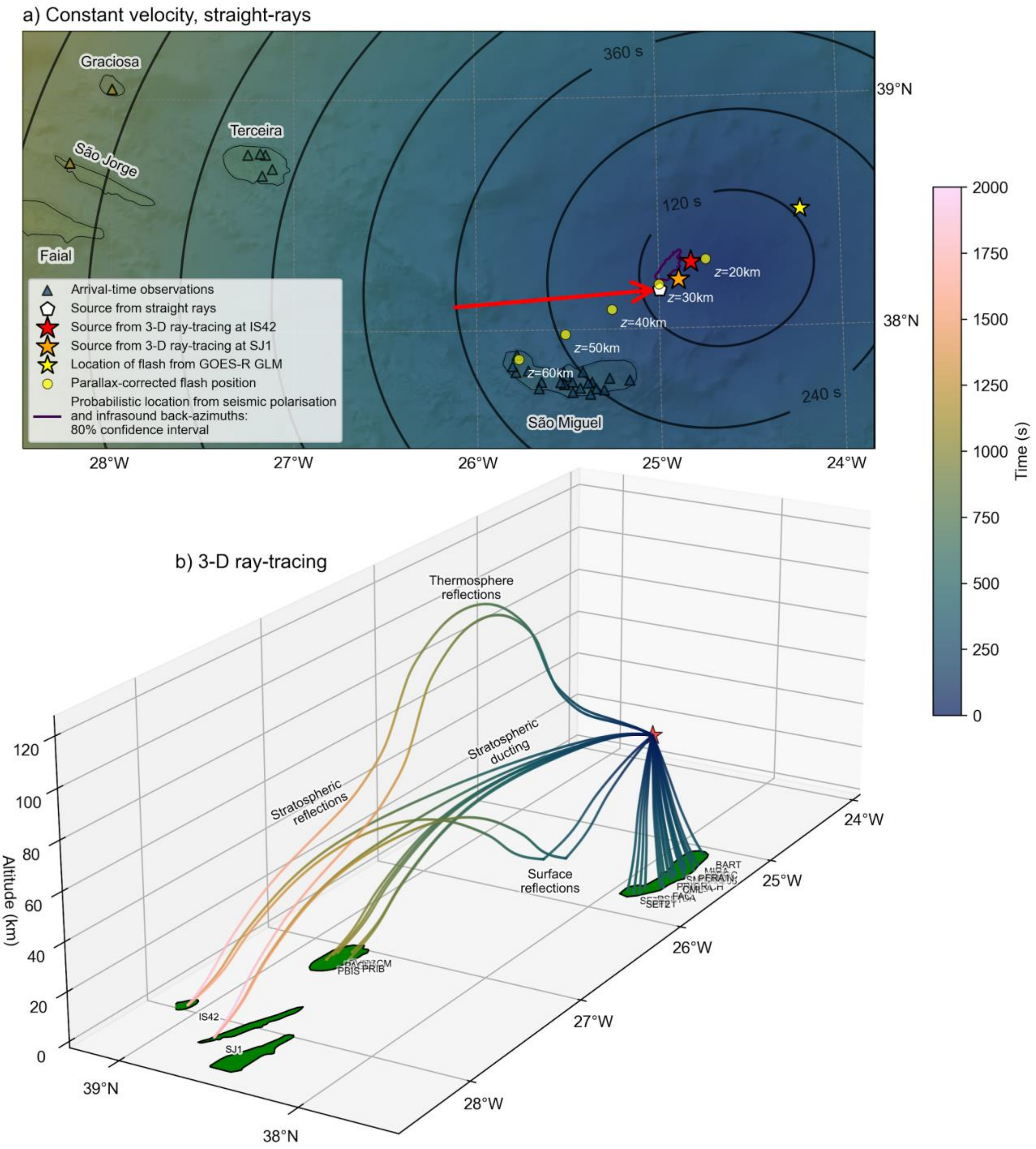

Figure 4: Meteoroid source models. a) Source position assuming straight rays in a constant velocity medium, with concentric contours representing the predicted arrival times. b) Perspective view from the SW of the source position derived using infrasound array data, displaying the 3-D raypaths traced in a realistic atmosphere model (coloured by time).

5. Discussion

5.1. Acoustic-seismic coupling mechanisms

Seismic waveform characteristics on São Miguel, a relatively small island (~60 km long), exhibit substantial variability at short distances (Figures 1 & 2a). Although there was no clear correlation between known site properties, the waveform variability due to different acoustic-to-seismic coupling properties must arise from multiple subtle site factors (Edwards et al., 2008; Hedlin & Walker, 2013; Kanamori et al., 1991; Stich et al., 2022). Monochromatic seismic waveforms (e.g., at CP.PVER) indicate air-coupled Rayleigh waves (Albert et al., 2013; Anthony et al., 2022; Edwards et al., 2007), while the weak precursory signals detected at PM.BART and PM.PGRON may represent *ground*-coupled Rayleigh waves (D'Auria et al., 2006; Edwards et al., 2008; Langston, 2004; Stich et al., 2022).

Initially, the colocated seismic and infrasound signals from II.CMLA demonstrate relatively good coherence for ~0.6 s (Figure S6). However, the infrasound signal is ~15 s shorter, again emphasising the role of local site effects. The absence of a π/2 phase shift supports the presence of air-coupled Rayleigh waves rather than direct pressure loading from the atmosphere (Anthony et al., 2022). The relatively low coupling transfer coefficient (Edwards et al., 2007; Novoselov et al., 2020) of 0.24 μm/s/Pa is consistent with the II.CMLA's location on a higher-rigidity lava flow (Anthony et al., 2022), but is contrary to the expectation that weaker acoustic-seismic coupling restricts the generation of air-coupled Rayleigh waves (Wills et al., 2022).

5.2. Size of the 2022 Azores Fireball

An outstanding question remains about the size of the fireball. Brown et al. (2007) suggest ~6x10^{-5} kt TNT equivalent as the minimum kinetic energy necessary for a meteoroid that is detectable by infrasound. To estimate the energy of the 2022 Azores fireball event, we used empirical relations (see e.g., Belli et al., 2021 and references therein). Our 3-D ray-tracing showed that the infrasound signal at II.CMLA on São Miguel results from direct raypaths through the stratosphere. Therefore, we can use the peak-to-peak amplitude size energy estimation of Whitaker (1995) that comes from explosion datasets, accounting for the wind speed along the raypath, and the horizontal distance between the source and receiver. With this relationship, we derive a kinetic energy of 5.6x10^{-3} kT TNT equivalent. For the more distant infrasound arrays on Graciosa (IS42) and São Jorge (SJ1), we used instead the period-based relationship of Revelle (1997) that accounts for wind velocity encountered along the raypath and source-receiver distance. Applying this relationship to the signals, we estimate a similar kinetic energy of 3.9x10^{-3} kT TNT equivalent.

We can also use the luminous energy from the GLM-derived light curve (Figure S5) by converting luminous energy into visual magnitude and impact energy, accounting for the GLM passband and the altitude of the source. We follow the method described by Ott et al. (2021), adapted from Jenniskens et al. (2018). We estimate an energy of 1.35x10^{-4} kT TNT equivalent. This energy equates to a visual magnitude of -13.8, close to the previously hypothesised minimum detection threshold of the GLM (Rumpf et al., 2019). The energies derived from infrasound are about an order of magnitude larger than that from the GLM data. Ott et al. (2021) noted a similar discrepancy. Such systemic infrasound-optical energy discrepancies should be taken into account by future studies on fireballs that utilise lightning mapper data.

Applying this range in energy estimates to the power laws given by Brown et al. (2002), we estimate that the meteoroid's diameter was ~0.12–0.40 m. It is thought that approximately ~11,000 to 400 objects of this size typically enter Earth's atmosphere each year

5.3. Implications for fireball detection

The flash was not identified as a fireball through automated processing of GLM data (Smith et al., 2021) or U.S. Government satellite data (https://cneos.jpl.nasa.gov/fireballs/) (Brown, Spalding, et al., 2002). In these automated detection pipelines, fireballs are identified by linear trajectories of individual flashes, and a light curve comprising greater energy release toward the end of the trajectory/flash event (Rumpf et al., 2019). However, from the locations of detection groups made up of individual events, there is no evidence for a systematic, linear trend in track, unlike other fireballs (Rumpf et al., 2019) (Figure S5). The 29 June 2022 event tracks over a small distance (<1 km), and the total flash duration is only 25 ms. Nor do we see a bias towards late energy disposition. These findings suggest that not all fireballs may conform to the characteristics identified by Rumpf et al. (2019). The lack of typical fireball source characteristics can be explained by parallax errors along the satellite's line-of-sight at the edge of its field of view, especially if the object's trajectory was in the look direction of the satellite.

A remaining issue is why the 2022 Azores fireball was not seen or heard by humans, even though skies were clear (Figure S1). Time of day can bias observations, yet many previous fireballs have been seen and heard in the early hours (Ott et al., 2020). The most densely populated parts of São Miguel are on the South coast - Ponta Delgada municipality and the neighbouring areas (Figure 1b). In contrast, the fireball was located ~60 km NE of São Miguel, and large volcanic edifices in the centre of the island may have partially obstructed the view of the fireball from the South.

6. Conclusions

Detailed seismoacoustic observations and modelling confirm a fireball source for the anomalous signal detected over the Azores in June 2022. The observed *W*-shapes in seismic waveforms are characteristic of a hypersonic or supersonic source. Array processing and 3-D ray-tracing of recorded infrasound pinpoint the terminal blast source at ~37 km altitude, ~60 km NE of São Miguel Island, consistent with seismic arrival times and polarisation directions. Multiple infrasound signals are consistent with different raypath geometries with reflections and multipathing effects, rather than indicating distinct sources. Our observations are reinforced by recordings from a satellite-based lightning detector, which crucially provided a high-precision source origin time. To our knowledge, the studied event is the first case of a fireball detected solely by a seismoacoustic network, rather than by human observers or *all-sky* cameras. The relatively weak energy of the event (~10^{-3} kT TNT equivalent) and its associated small diameter (~0.1–0.4 m) challenge the typically assumed energy thresholds for the automated detection of fireballs from geophysical and satellite data. Thus, combining data from satellites and co-located seismoacoustic stations can increase the geographic and temporal detection completeness for such relatively small fireballs, thousands of which enter Earth's atmosphere annually. By increasing our observational coverage, this combination of data sources could thus help to better understand atmosphere entry processes of small near-Earth objects, and ultimately improve models of the structure of the atmosphere.

Acknowledgements

AMG, SPH & MT acknowledge project UPFLOW which is funded by the Excellent Science programme of the European Research Council (Ref: 101001601). SBM is supported by the Fundação para a Ciência e Tecnologia (FCT) through the scholarship UI/BD/151384/2021. IVAR and CIVISA supported the installation and maintenance of the SJ1 infrasound array from the University of Florence on São Jorge Island.

Open Research

Data availability statement

Windowed seismic waveforms cut out 50 seconds before and after the fireball signal are openly available at the following Zenodo repository https://doi.org/10.5281/zenodo.8210656 (Hicks et al., 2023).

Original seismic data from the IPMA network (code: PM) is available through IPMA's FDSN web service client: http://ceida.ipma.pt. Original seismic data from the Global Seismographic Network (GSN) (Scripps Institution of Oceanography, 1986) for station II.CMLA was obtained through the IRIS Data Management Center (http://service.iris.edu).

Infrasound data from the SJ1 array of the Unifi network (code: FI) are available on the following Open Science Framework (OSF) repository: https://osf.io/987qv/. IMS data for the IS42 infrasound array are available from the CTBTO Preparatory Commission for scientific purposes through the virtual Data Exploitation Centre (vDEC): https://www.ctbto.org/resources/for-researchers-experts/vdec.

Original data from the GOES-16 Geostationary Lightning Mapper (GLM) was downloaded from NOAA's Comprehensive Large Array-data Stewardship System (CLASS) (https://www.avl.class.noaa.gov/). Infrared and cloud mask satellite data was obtained from EUMETSAT (https://data.eumetsat.int/).

Code availability statement

A Python Jupyter Notebook to reproduce the figures of this paper is available at the following Zenodo repository https://doi.org/10.5281/zenodo.8210656 (Hicks et al., 2023). Seismic waveform data was processed using ObsPy (Krischer et al., 2015). Colour palettes used for plotting come from the Scientific Colour Maps package (Crameri, 2020; Crameri et al., 2020). Satellite data was processed using the PyGrib (J. Whitaker et al., 2020), SatPy (Raspaud et al., 2023), and GOES (https://github.com/joaohenry23/GOES) Python packages.

Author contributions

Conceptualization: SPH, SBM, AP, MT, KH, AMGF.
Data curation: SPH, SBM, AP, GB, DG, MT, RAMS, NW.
Formal analysis: SPH, SBM, AP, GB, DG.
Funding acquisition: AMGF, NW, SBM.
Investigation: SPH, SBM, AP, GB, DG, MT, KH, WG, RAMS, NW, AMGF.
Methodology: SPH, SBM, AP, GB, DG.
Writing - original draft: SPH, SBM, AP, GB, DG.
Writing - editing & review: SPH, SBM, AMGF, GB, DG, KH, AP, NW

References

Albert, D. G., Taherzadeh, S., Attenborough, K., Boulanger, P., & Decato, S. N. (2013). Ground vibrations produced by surface and near-surface explosions. *Applied Acoustics*, *74*(11), 1279–1296. https://doi.org/10.1016/j.apacoust.2013.03.006

Anthony, R. E., Watzak, J., Ringler, A. T., & Wilson, D. C. (2022). Characteristics, relationships and precision of direct acoustic-to-seismic coupling measurements from local explosions. *Geophysical Journal International*, *230*(3), 2019–2035. https://doi.org/10.1093/gji/ggac154

Belli, G., Pace, E., & Marchetti, E. (2021). Detection and source parametrization of small-energy fireball events in Western Alps with ground-based infrasonic arrays. *Geophysical Journal International*, *225*(3), 1518–1529. https://doi.org/10.1093/gji/ggab042

Blom, P., & Waxler, R. (2012). Impulse propagation in the nocturnal boundary layer: Analysis of the geometric component. *The Journal of the Acoustical Society of America*, *131*(5), 3680–3690. https://doi.org/10.1121/1.3699174

Brown, P. G., ReVelle, D. O., Tagliaferri, E., & Hildebrand, A. R. (2002). An entry model for the Tagish Lake fireball using seismic, satellite and infrasound records. *Meteoritics & Planetary Science*, *37*(5), 661–675. https://doi.org/10.1111/j.1945-5100.2002.tb00846.x

Brown, P. G., Spalding, R. E., ReVelle, D. O., Tagliaferri, E., & Worden, S. P. (2002). The flux of small near-Earth objects colliding with the Earth. *Nature*, *420*(6913), 294–296. https://doi.org/10.1038/nature01238

Brown, P. G., Kalenda, P., Revelle, D. O., & Borovi̇̂cka, J. (2003). The Morávka meteorite fall: 2. Interpretation of infrasonic and seismic data. *Meteoritics & Planetary Science*, *38*(7), 989–1003. https://doi.org/10.1111/j.1945-5100.2003.tb00294.x

Brown, P. G., Edwards, W. N., ReVelle, D. O., & Spurny, P. (2007). Acoustic analysis of shock production by very high-altitude meteors—I: infrasonic observations, dynamics and luminosity. *Journal of Atmospheric and Solar-Terrestrial Physics*, *69*(4), 600–620. https://doi.org/10.1016/j.jastp.2006.10.011

Brown, P. G., McCAUSLAND, P. J. A., Fries, M., Silber, E., Edwards, W. N., Wong, D. K., et al. (2011). The fall of the Grimsby meteorite—I: Fireball dynamics and orbit from radar, video, and infrasound records. *Meteoritics & Planetary Science*, *46*(3), 339–363. https://doi.org/10.1111/j.1945-5100.2010.01167.x

Ceplecha, Z., Borovička, J., Elford, W. G., ReVelle, D. O., Hawkes, R. L., Porubčan, V., & Šimek, M. (1998). Meteor Phenomena and Bodies. *Space Science Reviews*, *84*(3), 327–471. https://doi.org/10.1023/A:1005069928850

Che, I.-Y., Kim, G., & Lee, H.-I. (2016). Seismic and infrasonic analysis of the 9 March 2014 fireball in South Korea. *Geosciences Journal*, *20*(2), 209–220. https://doi.org/10.1007/s12303-015-0034-1

Crameri, F. (2020, January 6). Scientific colour maps. Zenodo. https://doi.org/10.5281/zenodo.4153113

Crameri, F., Shephard, G. E., & Heron, P. J. (2020). The misuse of colour in science communication. *Nature Communications*, *11*(1), 5444. https://doi.org/10.1038/s41467-020-19160-7

D'Auria, L., Marotta, E., Martini, M., & Ricciolino, P. (2006). Seismic and acoustic detection of a bolide airburst in the Gulf of Naples (southern Italy). *Journal of Geophysical Research: Solid Earth*, *111*(B10). https://doi.org/10.1029/2005JB004254

Drob, D. P., Picone, J. M., & Garcés, M. (2003). Global morphology of infrasound propagation. *Journal of Geophysical Research: Atmospheres*, *108*(D21). https://doi.org/10.1029/2002JD003307

Drolshagen, E., Ott, T., Koschny, D., Drolshagen, G., Schmidt, A. K., & Poppe, B. (2020). Velocity distribution of larger meteoroids and small asteroids impacting Earth. *Planetary and Space Science*, *184*, 104869. https://doi.org/10.1016/j.pss.2020.104869

Edwards, W. N., Brown, P. G., & ReVelle, D. O. (2006). Estimates of meteoroid kinetic energies from observations of infrasonic airwaves. *Journal of Atmospheric and Solar-Terrestrial Physics*, *68*(10), 1136–1160. https://doi.org/10.1016/j.jastp.2006.02.010

Edwards, W. N., Eaton, D. W., McCausland, P. J., ReVelle, D. O., & Brown, P. G. (2007). Calibrating infrasonic to seismic coupling using the Stardust sample return capsule shockwave: Implications for seismic observations of meteors. *Journal of Geophysical Research: Solid Earth*, *112*(B10). https://doi.org/10.1029/2006JB004621

Edwards, W. N., Eaton, D. W., & Brown, P. G. (2008). Seismic observations of meteors: Coupling theory and observations. *Reviews of Geophysics*, *46*(4). https://doi.org/10.1029/2007RG000253

Flinn, E. A. (1965). Signal analysis using rectilinearity and direction of particle motion. *Proceedings of the IEEE*, *53*(12), 1874–1876. https://doi.org/10.1109/PROC.1965.4462

Gao, B., & Mathews, J. D. (2015). High-altitude meteors and meteoroid fragmentation observed at the Jicamarca Radio Observatory. *Monthly Notices of the Royal Astronomical Society*, *446*(4), 3404–3415. https://doi.org/10.1093/mnras/stu2176

de Groot-Hedlin, C., Hedlin, M. A. H., & Walker, K. (2011). Finite difference synthesis of infrasound propagation through a windy, viscous atmosphere: application to a bolide explosion detected by seismic networks. *Geophysical Journal International*, *185*(1), 305–320. https://doi.org/10.1111/j.1365-246X.2010.04925.x

Halliday, I., Blackwell, A. T., & Griffin, A. A. (1989). The typical meteorite event, based on photographic records of 44 fireballs. *Meteoritics*, *24*(2), 65–72. https://doi.org/10.1111/j.1945-5100.1989.tb00946.x

Hedlin, M. A. H., & Walker, K. T. (2013). A study of infrasonic anisotropy and multipathing in the atmosphere using seismic networks. *Philosophical Transactions of the Royal Society A: Mathematical, Physical and Engineering Sciences*, *371*(1984), 20110542. https://doi.org/10.1098/rsta.2011.0542

Hedlin, M. A. H., Drob, D., Walker, K., & de Groot-Hedlin, C. (2010). A study of acoustic propagation from a large bolide in the atmosphere with a dense seismic network. *Journal of Geophysical Research: Solid Earth*, *115*(B11). https://doi.org/10.1029/2010JB007669

Hicks, S., Matos, S., Pimentel, A., Belli, G., Gheri, D., Tsekhmistrenko, M., et al. (2023). Supplementary Data and Codes for “Exclusive seismoacoustic detection and characterisation of an unseen and unheard fireball in the North Atlantic” by Stephen P. Hicks and Sandro B. Matos, et al. [Data set]. Zenodo. https://doi.org/10.5281/zenodo.8210656

Hughes, A., Sankar, R., Davis, K. E., Palotai, C., & Free, D. L. (2022). Analysis of the April 13, 2021 bolide off the coast of Florida and Grand Bahama Island. *Meteoritics & Planetary Science*, *57*(3), 575–587. https://doi.org/10.1111/maps.13781

Instituto Português do Mar e da Atmosfera, I.P. (2006). Portuguese National Seismic Network [SEED data]. International Federation of Digital Seismograph Networks. https://doi.org/10.7914/SN/PM

Ishihara, Y., Tsukada, S., Sakai, S., Hiramatsu, Y., & Furumoto, M. (2003). The 1998 Miyako fireball’s trajectory determined from shock wave records of a dense seismic array. *Earth, Planets and Space*, *55*(5), e9–e12. https://doi.org/10.1186/BF03351752

Jenniskens, P., Albers, J., Tillier, C. E., Edgington, S. F., Longenbaugh, R. S., Goodman, S. J., et al. (2018). Detection of meteoroid impacts by the Geostationary Lightning Mapper on the GOES-16 satellite. *Meteoritics & Planetary Science*, *53*(12), 2445–2469. https://doi.org/10.1111/maps.13137

Kanamori, H., Mori, J., Anderson, D. L., & Heaton, T. H. (1991). Seismic excitation by the space shuttle Columbia. *Nature*, *349*(6312), 781–782. https://doi.org/10.1038/349781a0

Krischer, L., Megies, T., Barsch, R., Beyreuther, M., Lecocq, T., Caudron, C., & Wassermann, J. (2015). ObsPy: a bridge for seismology into the scientific Python ecosystem. *Computational Science & Discovery*, *8*(1), 014003. https://doi.org/10.1088/1749-4699/8/1/014003

Kumar, U., Chao, B. F., Hsieh, Y., & Chang, E. T. Y. (2017). A meteor shockwave event recorded at seismic and infrasound stations in northern Taiwan. *Geoscience Letters*, *4*(1), 13. https://doi.org/10.1186/s40562-017-0079-2

Langston, C. A. (2004). Seismic ground motions from a bolide shock wave. *Journal of Geophysical Research: Solid Earth*, *109*(B12). https://doi.org/10.1029/2004JB003167

Llorca, J., Trigo-Rodríguez, J. M., Ortiz, J. L., Docobo, J. A., García-Guinea, J., Castro-Tirado, A. J., et al. (2005). The Villalbeto de la Peña meteorite fall: I. Fireball energy, meteorite recovery, strewn field, and petrography. *Meteoritics & Planetary Science*, *40*(6), 795–804. https://doi.org/10.1111/j.1945-5100.2005.tb00155.x

Novoselov, A., Fuchs, F., & Bokelmann, G. (2020). Acoustic-to-seismic ground coupling: coupling efficiency and inferring near-surface properties. *Geophysical Journal International*, *223*(1), 144–160. https://doi.org/10.1093/gji/ggaa304

Ott, T., Drolshagen, E., Koschny, D., Drolshagen, G., Pilger, C., Mialle, P., et al. (2020). NEMO - The NEar real-time MOnitoring system – Harvesting information online for a fireball monitoring and alert system. *Acta Astronautica*, *177*, 172–181. https://doi.org/10.1016/j.actaastro.2020.07.013

Ott, T., Drolshagen, E., Koschny, D., Drolshagen, G., Pilger, C., Gaebler, P., et al. (2021). Infrasound signals of fireballs detected by the Geostationary Lightning Mapper. *Astronomy & Astrophysics*, *654*, A98. https://doi.org/10.1051/0004-6361/202141106

Pujol, J., Rydelek, P., & Bohlen, T. (2005). Determination of the Trajectory of a Fireball Using Seismic Network Data. *Bulletin of the Seismological Society of America*, *95*(4), 1495–1509. https://doi.org/10.1785/0120040155

Pujol, J., Rydelek, P., & Ishihara, Y. (2006). Analytical and graphical determination of the trajectory of a fireball using seismic data. *Planetary and Space Science*, *54*(1), 78–86. https://doi.org/10.1016/j.pss.2005.08.003

Raspaud, M., Hoese, D., Lahtinen, P., Holl, G., Finkensieper, S., Proud, S., et al. (2023, February 9). pytroll/satpy: Version 0.40.0 (2023/02/09). Zenodo. https://doi.org/10.5281/zenodo.7624532

Revelle, D. O. (1976). on meteor-generated infrasound. *Journal of Geophysical Research (1896-1977)*, *81*(7), 1217–1230. https://doi.org/10.1029/JA081i007p01217

ReVelle, D. O. (1997). Historical Detection of Atmospheric Impacts by Large Bolides Using Acoustic-Gravity Waves a. *Annals of the New York Academy of Sciences*, *822*(1), 284–302.

Rumpf, C. M., Longenbaugh, R. S., Henze, C. E., Chavez, J. C., & Mathias, D. L. (2019). An Algorithmic Approach for Detecting Bolides with the Geostationary Lightning Mapper. *Sensors*, *19*(5), 1008. https://doi.org/10.3390/s19051008

Schwaiger, H. F., Iezzi, A. M., & Fee, D. (2019). AVO-G2S: A modified, open-source Ground-to-Space atmospheric specification for infrasound modeling. *Computers & Geosciences*, *125*, 90–97. https://doi.org/10.1016/j.cageo.2018.12.013

Scripps Institution of Oceanography. (1986). Global Seismograph Network - IRIS/IDA [SEED data]. International Federation of Digital Seismograph Networks. https://doi.org/10.7914/SN/II

Silber, E. A., & Brown, P. G. (2014). Optical observations of meteors generating infrasound—I: Acoustic signal identification and phenomenology. *Journal of Atmospheric and Solar-Terrestrial Physics*, *119*, 116–128. https://doi.org/10.1016/j.jastp.2014.07.005

Smith, J. C., Morris, R. L., Rumpf, C., Longenbaugh, R., McCurdy, N., Henze, C., & Dotson, J. (2021). An automated bolide detection pipeline for GOES GLM. *Icarus*, *368*, 114576. https://doi.org/10.1016/j.icarus.2021.114576

Stähler, S. C., Zenhäusern, G., Clinton, J., & Giardini, D. (2022). Locating the Nordstream explosions using polarization analysis. *Seismica*, *1*(1). https://doi.org/10.26443/seismica.v1i1.253

Stich, D., Rabasco, J. C., Madiedo, J. M., Guerrero Rascado, J. L., & Soto, J. M. (2022). Seismic observation and location of a meteor burst from a dense station deployment in Southern Spain. *Geophysical Research Letters*, *n/a*(n/a), e2022GL099999. https://doi.org/10.1029/2022GL099999

Tatum, J. B. (1999). Fireballs: Interpretation of airblast data. *Meteoritics & Planetary Science*, *34*(4), 571–585. https://doi.org/10.1111/j.1945-5100.1999.tb01364.x

Ulivieri, G., Marchetti, E., Ripepe, M., Chiambretti, I., De Rosa, G., & Segor, V. (2011). Monitoring snow avalanches in Northwestern Italian Alps using an infrasound array. *Cold Regions Science and Technology*, *69*(2), 177–183. https://doi.org/10.1016/j.coldregions.2011.09.006

Vera Rodriguez, I., Isken, M. P., Dahm, T., Lamb, O. D., Wu, S., Kristjánsdóttir, S., et al. (2022). Acoustic Signals of a Meteoroid Recorded on a Large-N Seismic Network and Fiber-Optic Cables. *Seismological Research Letters*. https://doi.org/10.1785/0220220236

Virts, K. S., & Koshak, W. J. (2020). Mitigation of Geostationary Lightning Mapper Geolocation Errors. *Journal of Atmospheric and Oceanic Technology*, *37*(9), 1725–1736. https://doi.org/10.1175/JTECH-D-19-0100.1

Walker, K. T., Hedlin, M. A. H., de Groot-Hedlin, C., Vergoz, J., Le Pichon, A., & Drob, D. P. (2010). Source location of the 19 February 2008 Oregon bolide using seismic networks and infrasound arrays. *Journal of Geophysical Research: Solid Earth*, *115*(B12). https://doi.org/10.1029/2010JB007863

Whitaker, J., Engle, E., Kemetmüller, J., Kemenade, H. van, Zackrisson, M., Thorsteinsson, H., et al. (2020, November 27). jswhit/pygrib: version 2.0.6 release. Zenodo. https://doi.org/10.5281/zenodo.4292914

Whitaker, R. W. (1995). *Infrasonic monitoring*. Los Alamos National Lab.(LANL), Los Alamos, NM (United States).

Wills, G., Nippress, A., Green, D. N., & Spence, P. J. (2022). Site-specific variations in air-to-ground coupled seismic arrivals from the 2012 October 16 explosion at Camp Minden, Louisiana, United States. *Geophysical Journal International*, *231*(1), 243–255. https://doi.org/10.1093/gji/ggac184

Yamada, M. (2021). Determining the Source of the Explosive Sound Heard in Hokkaido, Japan, on 26 April 2021. *Journal of Geophysical Research: Solid Earth*, *126*(12), e2021JB023076. https://doi.org/10.1029/2021JB023076

Yamada, M., & Mori, J. (2012). Trajectory of the August 7, 2010 Biwako fireball determined from seismic recordings. *Earth, Planets and Space*, *64*(1), 27–35. https://doi.org/10.5047/eps.2011.08.021

Supplementary Information

Text S1: Infrasound array details

IS42. Infrasound records of this event were recorded by IS42 (39.04°N, 28.01°W), one of the International Monitoring System (IMS) of the Comprehensive Test Ban Treaty Organization (CTBTO) infrasound stations, located in dense forested area in the central part of Graciosa Island on the Azores Archipelago (Figure 1). Station IS42 is a 1.6 km aperture pentagon-shaped main array and a 200 m aperture inner sub-array. The array is composed of eight high-frequency MB2005 absolute pressure microbarometers capable of detecting pressure differences in the atmosphere of less than 1 mPa. The instrumental noise level is less than 2 mPa RMS within the 0.02–4 Hz, giving each sensor a dynamic range of 134 dB for a sensitivity of 1 mV/Pa. The sampling rate is 20 Hz. To reduce the wind noise to minimize pressure changes, four rosette-shaped Wind-Noise Reduction System (WNRS) equipped with 96 inlet ports was connected to each sensor. Also, the levelled ground stainless-steel pipes of WNRS are covered with a 0.10 m thick layer of 0.02 m size gravel to reduce wind turbulence and increase thermal insulation. All sensors are connected to the Central Facility (CF) with optical fibre, where data are received and sent by satellite to CTBTO-IMS headquarters in Vienna.

SJ1. Data recorded by the SJ1 portable infrasonic array, deployed on São Jorge Island near Rosais (38.72°N, 28.23°W) (Figure 1) since April 2022, as the result of a collaboration between the IVAR of the University of the Azores and the Department of Earth Science of the University of Florence, through the IVAR Academy programme. The array consists of four infrasonic sensors installed on a triangular geometry with an aperture (maximum distance between two elements) of ~140 m, optimised to analyse infrasound signals in the 1–10 Hz frequency band. Each array element is equipped with a differential pressure transducer with a sensitivity of 400 mV/Pa in the pressure range of ±12.5 Pa and a flat frequency response between 0.01 and 200 Hz. Analogue pressure data are sampled by the Guralp CMG-DM24 digitizer at 50 Hz and digitised at 16 bits. To reduce wind noise, each sensor is installed inside a plastic box buried in the ground within a flat forested area.

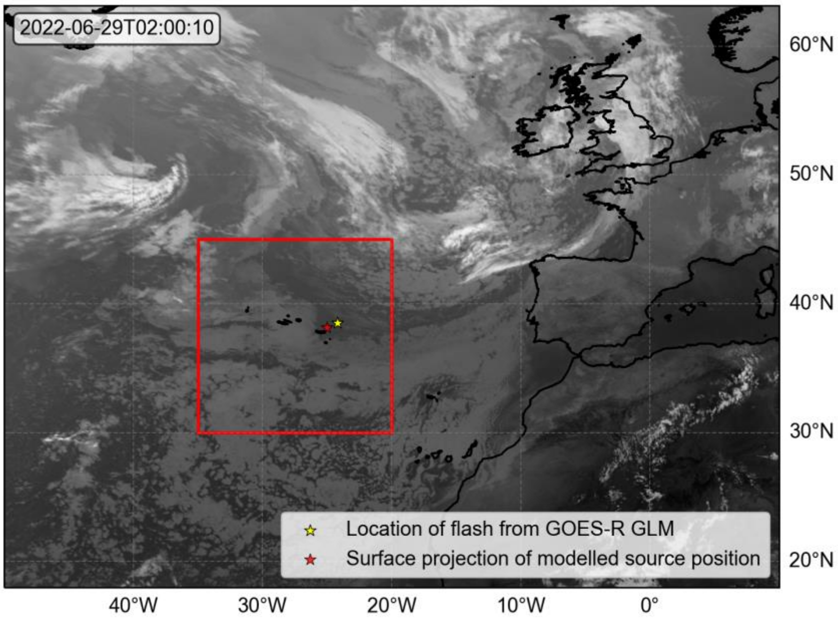

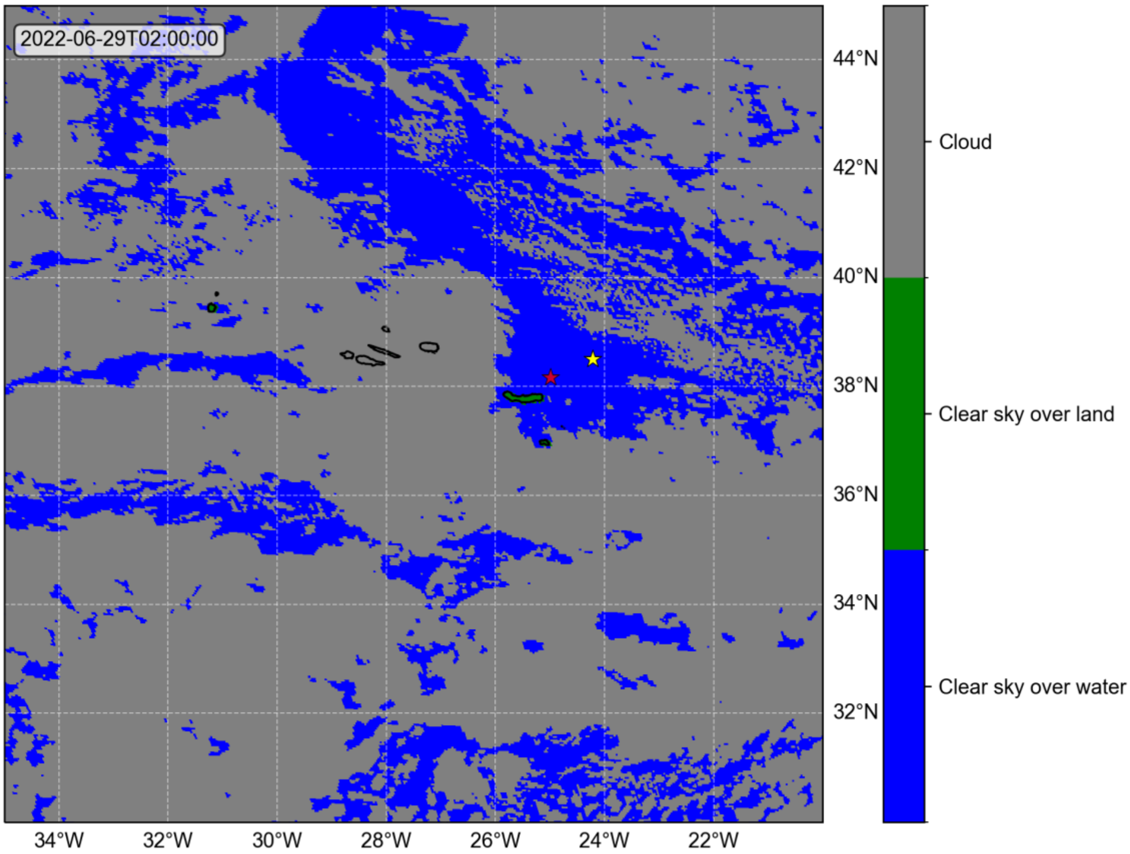

Figure S1: Top: Infrared image from the Meteosat Second Generation (MSG) satellite's Rapid Scan High Rate SEVIRI IR 3.9 product. The red box shows the location of the map in the bottom panel. Bottom: Cloud cover classification. Both products were downloaded from EUMETSAT (see Data Availability statement). The time in UTC of each image is given in the top-left corner. The coastlines are in black.

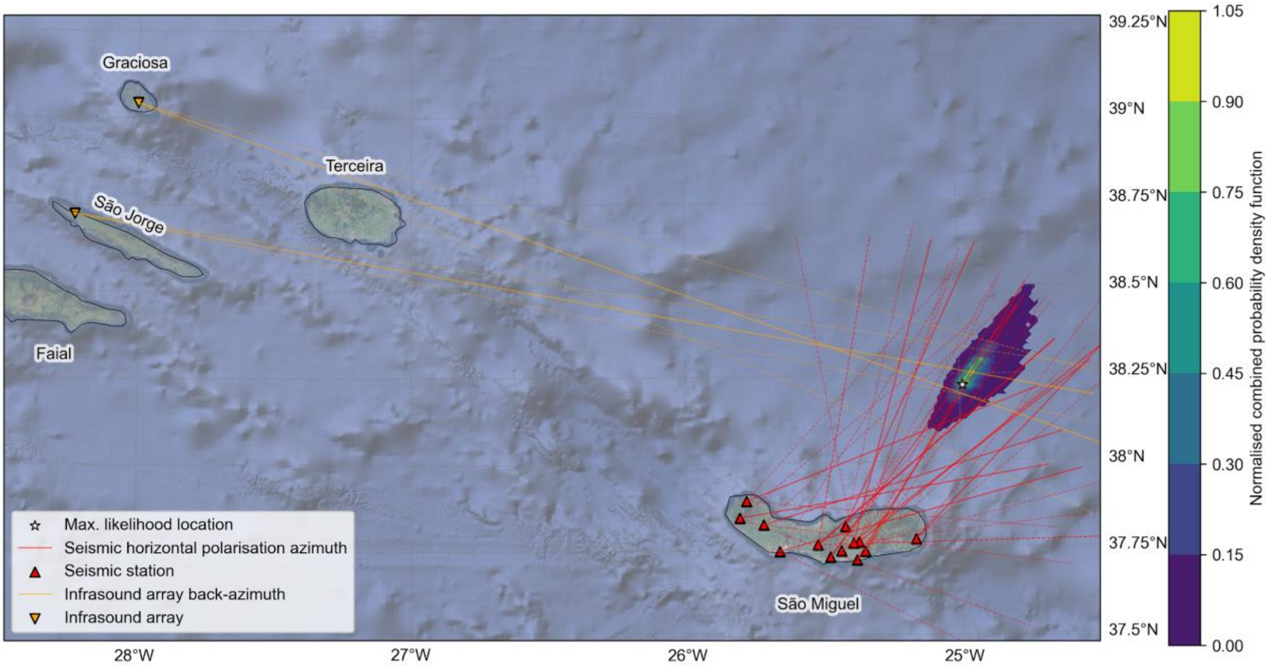

Figure S2: Azimuths and associated uncertainties from horizontal polarisation analysis of three-component seismic waveforms and infrasound array data. The coloured area shows the combined probability density function from all these azimuths, showing a tightly-constrained source position ~60 NE of São Miguel Island.

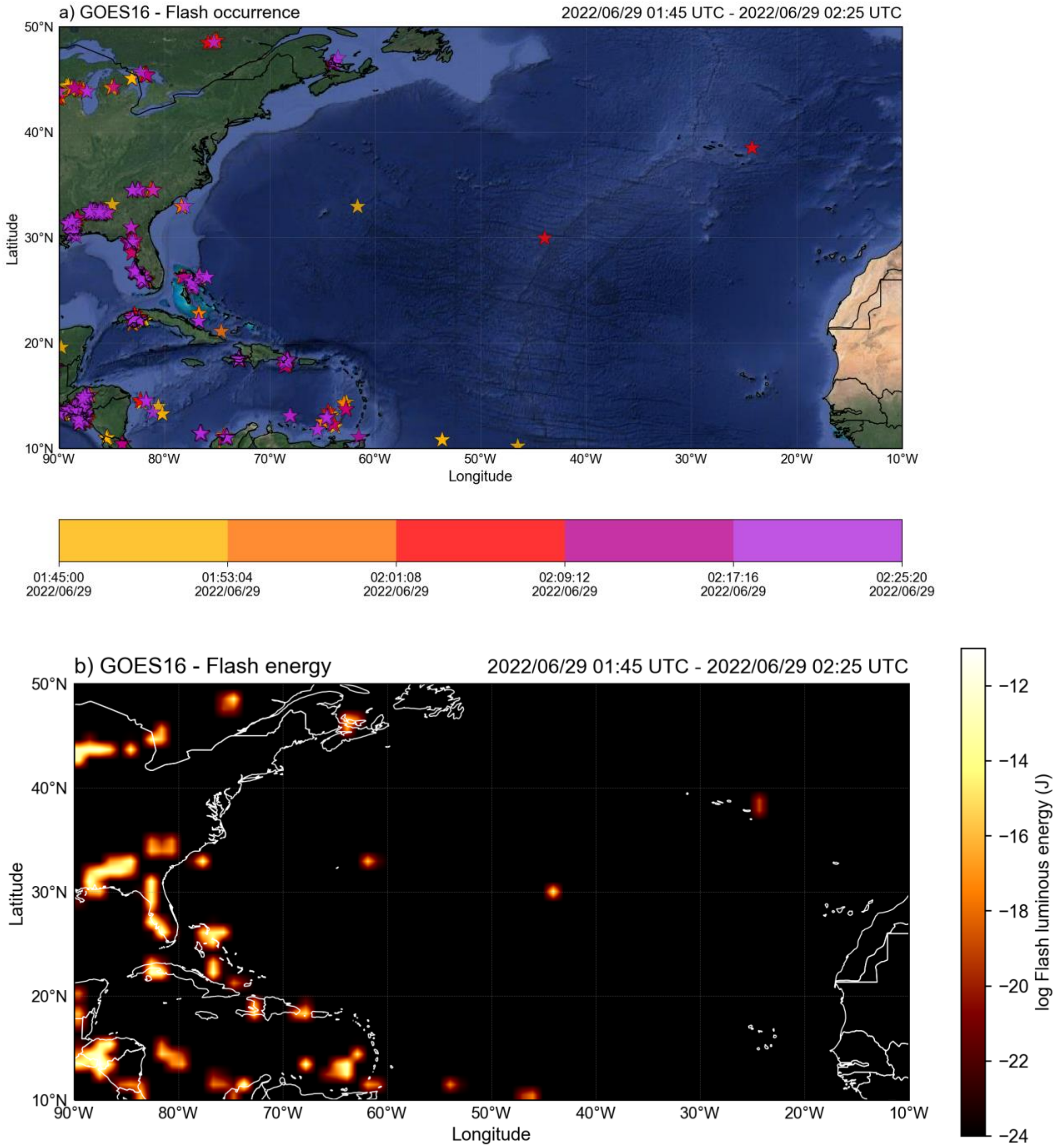

Figure S3: Geostationary Lightning Mapper (GLM) flash event detections roughly 15 mins before and after the observed seismic-acoustic signal. a) Individual detections coloured by flash time. b) Visualisation of total flash luminous energy based on Gaussian kernels with a standard deviation of 0.1°.

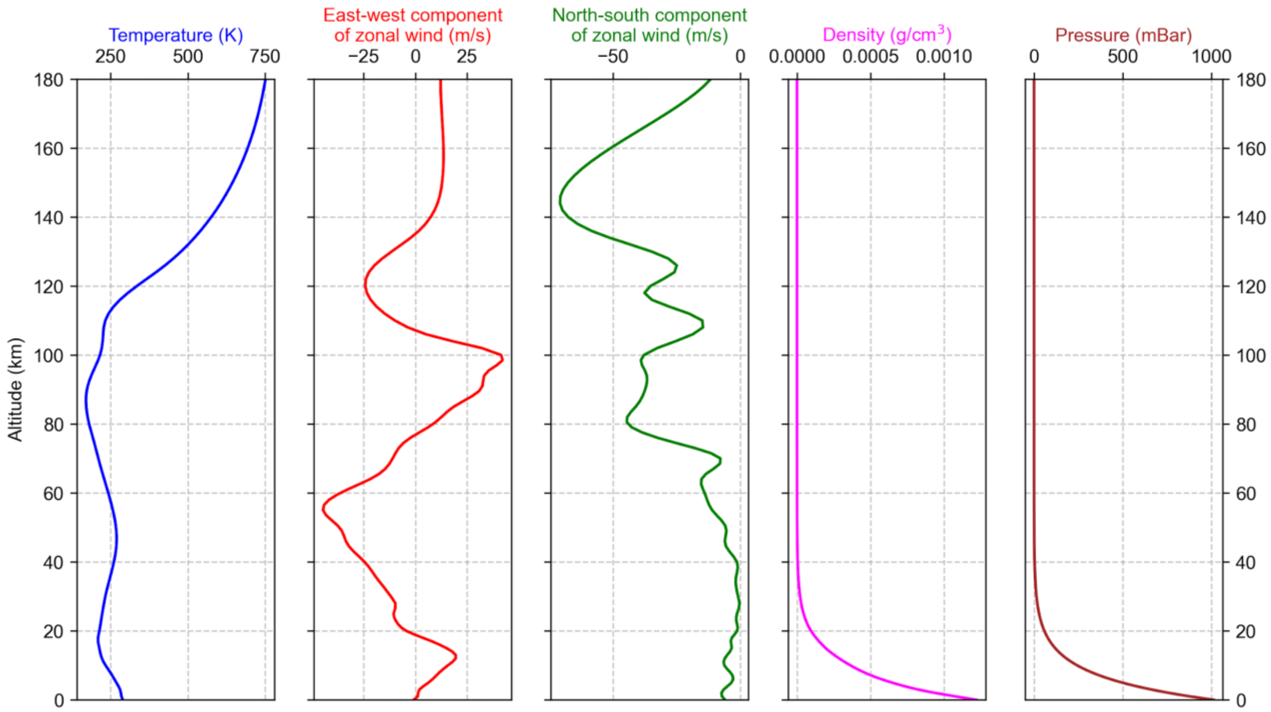

Figure S4: 1-D atmosphere model for a vertical profile located above Mosteiros on the West coast of São Miguel, based on 2.5° resolution data from the National Centers for Environmental Prediction (NCEP). The model has a vertical resolution of 1 km in the lower 20 km and 2.5 km between 20-180 km altitude.

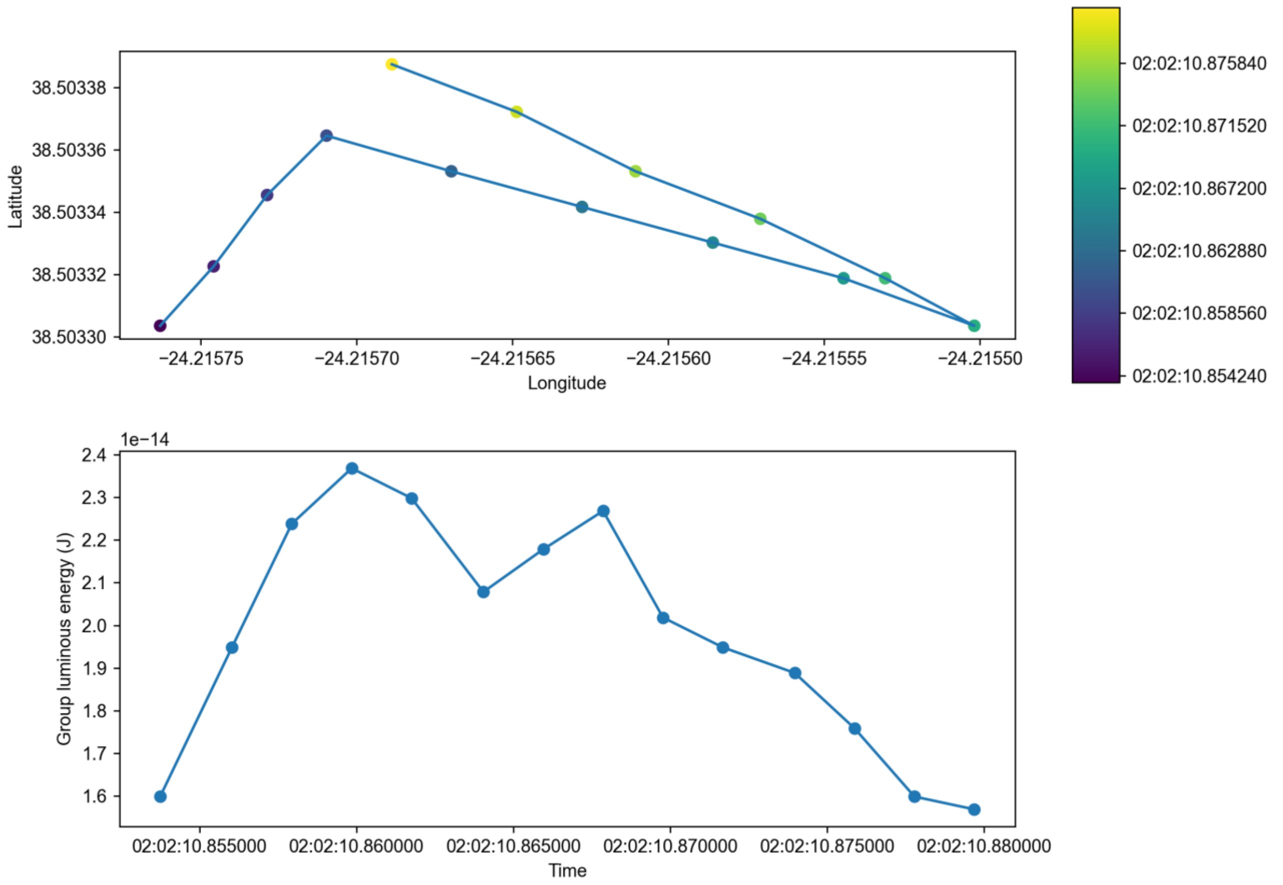

Figure S5: Geostationary Lightning Mapper (GLM) data for the 29 June 2022 Azores event. Top: Ground track plot, with points coloured by absolute time. Bottom: light curve over time. Each point represents a group of events that collectively constitute a total flash.

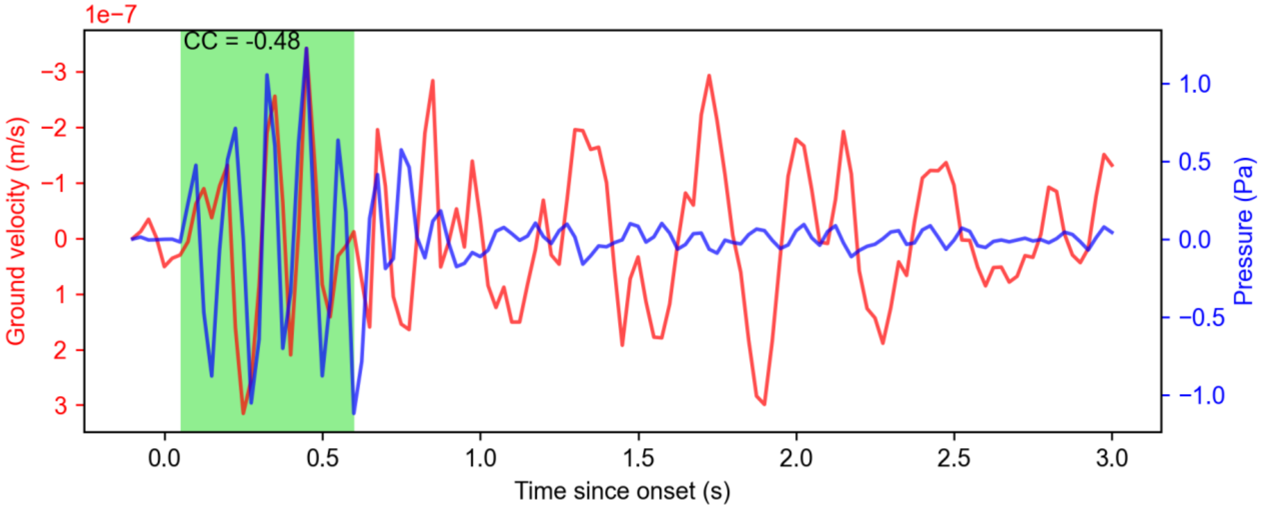

Figure S6: Waveform comparison between pressure and vertical ground velocity at II.CMLA. Note that the ground velocity scale has been inverted for easier visual comparison between the two measurements. Both sets of waveforms have been bandpass filtered between 2.5 and 18 Hz due to signal-to-noise ratio limitations on the ground velocity trace.

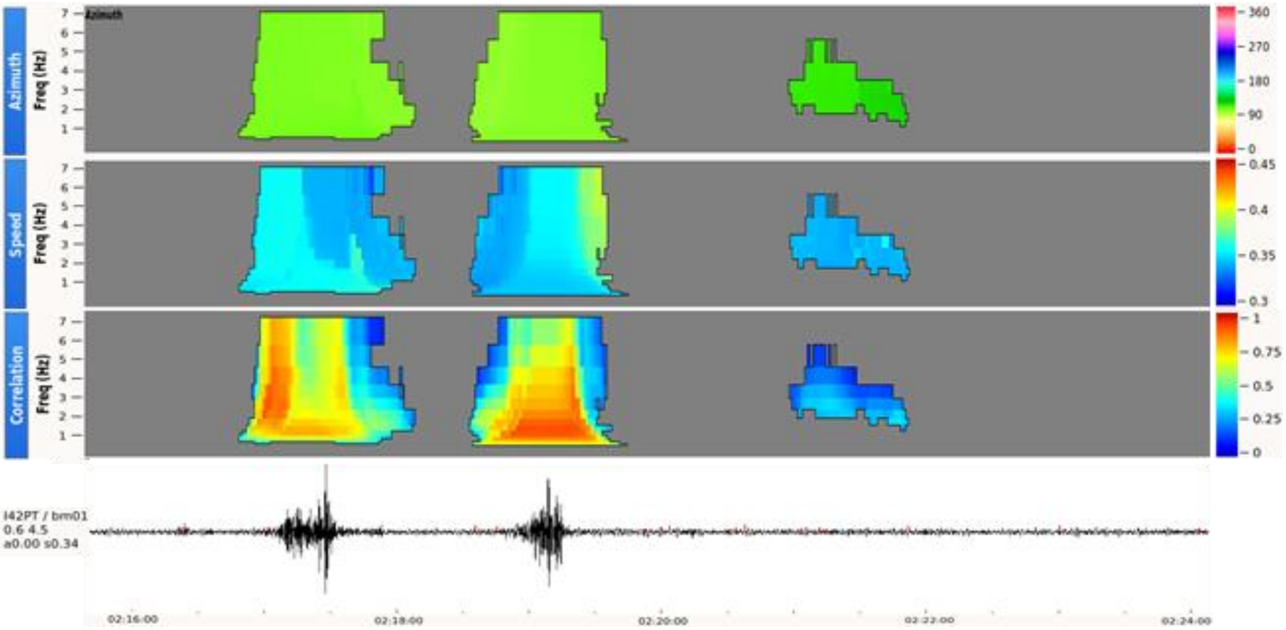

Figure S7: Progressive Multi-Channel Correlation algorithm (PMCC) computed results of infrasound records at IS42. For later calculation of the wave parameters, data were processed with the interactive analysis tool, DTK-GPMCC (Commissariat à l'Énergie Atomique/Département Analyse, Surveillance, Environment, France - CEA/DASE), integrated into the NDC-in-a-Box, v. 4.0 package, supplied by the International Data Centre. Three wave trains are shown but only the first two are clearly visible in the filtered amplitudes. Data are filtered from 0.6 to 4.5 Hz in 19 one-third Octave frequency bands. Back-azimuths, horizontal trace velocity (km/s) and correlation for the three coherent detected signals are shown by the colour scales on the right.

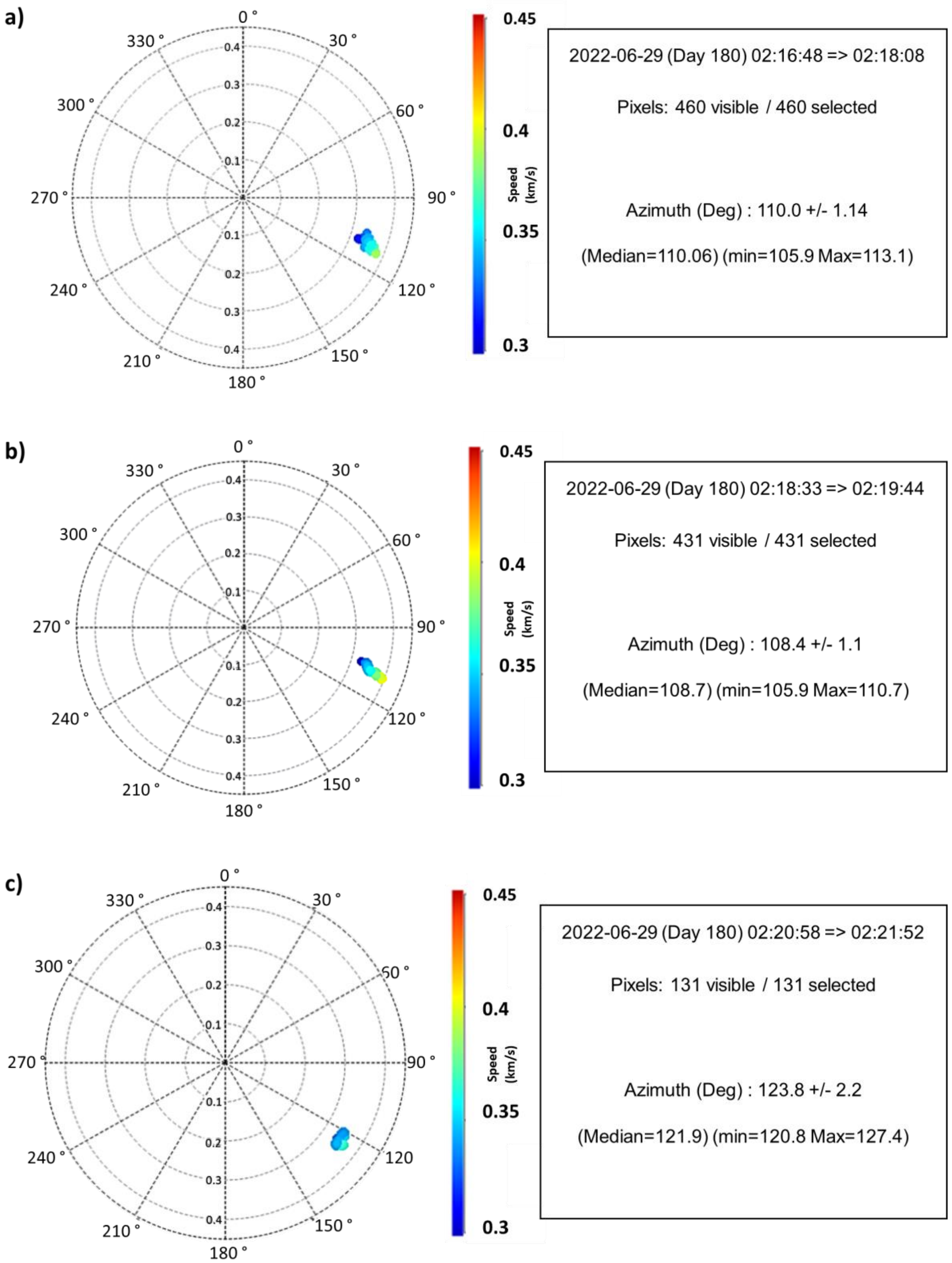

2022-06-29 (Day 180) 02:16:48 => 02:18:08

Pixels: 460 visible / 460 selected

Azimuth (Deg) : 110.0 +/- 1.14

(Median=110.06) (min=105.9 Max=113.1)

2022-06-29 (Day 180) 02:18:33 => 02:19:44

Pixels: 431 visible / 431 selected

Azimuth (Deg) : 108.4 +/- 1.1

(Median=108.7) (min=105.9 Max=110.7)

2022-06-29 (Day 180) 02:20:58 => 02:21:52

Pixels: 131 visible / 131 selected

Azimuth (Deg) : 123.8 +/- 2.2

(Median=121.9) (min=120.8 Max=127.4)

Figures S8: - IS42 infrasound station polar plots according to azimuth (polar angle) and horizontal trace velocity (polar radius) related to the three wavetrains recorded in the infrasound station IS42: a) The first wave train back-azimuths span from 105.9° to 113.1°; b) Second wavetrain back-azimuths span from 105.9° to 110.7°; c) Third wavetrain back-azimuths span from 120.8° to 127.4°.

Parameter	**Lower bound**	**Upper bound**
Object velocity (km/s)	10	45
Source easting (km)	-50	350
Source northing (km)	0	350
Source elevation (km)	20	60
Trajectory azimuth	0	360
Trajectory inclination	0	90

Table S1: Parameter lower and upper bounds used for the trajectory optimisation using the straight-ray (constant velocity) approach. Horizontal source positions are given in a cartesian coordinate system relative to station PM.BART (37.78°N, -25.17°W).